

Article

Self-Powered Photoelectrochemical Assay for Hg²⁺ Detection Based on g-C₃N₄-CdS-CuO Composites and Redox Cycle Signal Amplification Strategy

Yonghuan Su ¹, Lixia Su ¹, Bingqian Liu ^{1,*} , Youxiu Lin ² and Dianping Tang ^{3,*} 

¹ Guizhou Engineering Laboratory for Synthetic Drugs (Ministry of Education of Guizhou Province), College of Pharmacy, Guizhou University, Guiyang 550025, China; gs.yhsu20@gzu.edu.cn (Y.S.); gs.lxsu20@gzu.edu.cn (L.S.)

² Key Laboratory of Modern Analytical Science and Separation Technology of Fujian Province, College of Chemistry, Chemical Engineering and Environment, Minnan Normal University, Zhangzhou 363000, China; lyx1817@mnnu.edu.cn

³ Key Laboratory of Analytical Science for Food Safety and Biology (MOE & Fujian Province), Department of Chemistry, Fuzhou University, Fuzhou 350108, China

* Correspondence: nqliu@gzu.edu.cn (B.L.); dianping.tang@fzu.edu.cn (D.T.); Tel.: +86-591-22866125 (D.T.)

Abstract: A highly sensitive self-powered photoelectrochemical (spPEC) sensing platform was constructed for Hg²⁺ determination based on the g-C₃N₄-CdS-CuO co-sensitized photoelectrode and a visible light-induced redox cycle for signal amplification. Through successively coating the single-layer g-C₃N₄, CdS, and CuO onto the surface of an electrode, the modified electrode exhibited significantly enhanced PEC activity. The microstructure of the material was characterized by scanning electron microscopy (SEM), X-ray diffraction (XRD) and Fourier transform infrared spectroscopy (FT-IR). However, the boost in photocurrent could be noticeably suppressed due to the consumption of hole-scavenging agents (reduced glutathione) by the added Hg²⁺. Under optimal conditions, we discovered that the photocurrent was linearly related to the Hg²⁺ concentration in the range of 5 pM–100 nM. The detection limit for Hg²⁺ was 0.84 pM. Moreover, the spPEC sensor demonstrated good performance for the detection of mercury ions in human urine and artificial saliva.

Keywords: g-C₃N₄-CdS-CuO composites; self-powered photoelectrochemical assay; Hg²⁺ detection; redox cycle signal amplification



Citation: Su, Y.; Su, L.; Liu, B.; Lin, Y.; Tang, D. Self-Powered Photoelectrochemical Assay for Hg²⁺ Detection Based on g-C₃N₄-CdS-CuO Composites and Redox Cycle Signal Amplification Strategy. *Chemosensors* **2022**, *10*, 286. <https://doi.org/10.3390/chemosensors10070286>

Academic Editor: Tae Geun Kim

Received: 26 May 2022

Accepted: 17 July 2022

Published: 18 July 2022

Publisher's Note: MDPI stays neutral with regard to jurisdictional claims in published maps and institutional affiliations.



Copyright: © 2022 by the authors. Licensee MDPI, Basel, Switzerland. This article is an open access article distributed under the terms and conditions of the Creative Commons Attribution (CC BY) license (<https://creativecommons.org/licenses/by/4.0/>).

1. Introduction

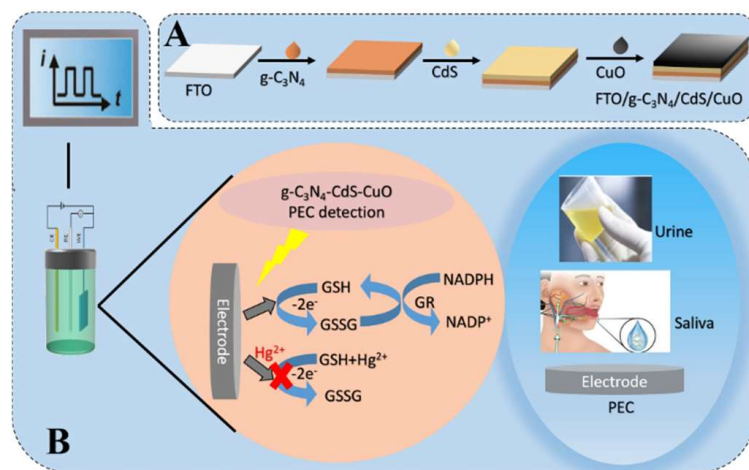
It is well known that heavy metals are very harmful to the human body. Among such metals, mercury is the most widely used heavy metal, and it is used in the manufacture of compact fluorescent-lamp light bulbs, jewelry, thermometers, blood pressure monitors, and silver dental fillings [1]. Mercury ions (Hg²⁺) are the general form of mercury and these can cause various diseases, such as hypertension, enteritis, bronchitis, and pulmonary edema [2]. At present, several methods have been utilized for the detection of mercury ions, including fluorescent and colorimetric sensors [3–5], surface-enhanced Raman scattering [6], and electrochemistry [7,8]. Although these methods have the advantages of high sensitivity and accuracy [9], they are limited by complex sample pretreatment and high operation cost [10]. Therefore, developing a mercury-ion detection method with a facile pretreatment process, and low cost, is imperative.

Photoelectrochemical (PEC) sensors demonstrate significant potential for analysis owing to advantages such as weak background noise, simple operation, high sensitivity, and quick response [11]. The self-powered photoelectrochemical (spPEC) sensor is an emerging photoelectrochemical detection method owing to its portability, lack of external power supply, and sustainability [12]. The spPEC sensor is primarily based on a three-electrode system, including the type of anode or cathode. The three-electrode scheme adopts a single

working electrode as the signal source and a specific recognition platform [13]. However, the interaction between the optical electrode and the reducing agent or the target molecule inevitably leads to deterioration of the performance of the PEC sensor [14]. Cao et al. [15] constructed an ingenious visible light-induced membraneless self-powered PEC biosensing platform by integrating a signal amplification strategy for PEC bioanalysis. Owing to the simple enzyme-induced chemical redox cycle process, the signal could be effectively and repeatedly regenerated through coupling reduction and oxidation reactions, which were used for ultrasensitive PEC analysis.

Therein, the selection of photoactive materials is the key to improving the detection of photoelectrochemical sensors. Currently, $g\text{-C}_3\text{N}_4$ is considered as the photoactive material with the highest potential owing to its advantages such as suitable band gap, excellent stability, and low toxicity [16]. Nevertheless, the photocatalytic efficiency of single-phase $g\text{-C}_3\text{N}_4$ is low owing to the lack of surface redox active sites and the high recombination rate of electron–hole (e^- - h^+) pairs [17]. To effectively improve the photocatalytic activity of $g\text{-C}_3\text{N}_4$, it is generally combined with other photoactive materials with lower band gaps. As n-type narrow-band gap semiconductors, CdS quantum dots (QDs) are often used for the study of visible light-active materials [18]. However, CdS QDs are not only photocorrosive [19] but also exhibit a high electron–hole recombination rate [20], which can be resolved by combining them with other p-type photoactive materials. CuO nanoparticles (NPs) are p-type semiconductors [21] that have been widely employed as photocatalysts for different reactions owing to their high conductivity and low band gap [22]. Therefore, combining n-type CdS and p-type CuO to form composites [23] may serve as an effective strategy for enhancing stability and inhibiting electron–hole recombination.

Herein, we propose a spPEC assay for Hg^{2+} detection based on $g\text{-C}_3\text{N}_4\text{-CdS-CuO}$ composites and a redox cycle signal amplification strategy. As presented in Scheme 1A, the $g\text{-C}_3\text{N}_4\text{-CdS-CuO}$ material is prepared via layer-by-layer self-assembly as a self-powered system. A fluorine-doped tin oxide (FTO) electrode is modified using the composite material as a photoanode. As illustrated in Scheme 1B, under irradiation, glutathione (GSH) is oxidized by CuO to form oxidized glutathione (GSSG) for generating a strong photocurrent owing to the GSH-oxidase and peroxidase-like activities of CuO NPs [24,25]. In the presence of GSH reductase (GR), GSSG is reduced to GSH using a reductive coenzyme II (NADPH) as a substrate, resulting in a redox cycle system [26], signal amplification is achieved through redox cycle. However, in the presence of Hg^{2+} , GSH can bind to Hg^{2+} based on the hard–soft acid–base (HSAB) theory [27], which influences the above redox cycle system and significantly reduces the photocurrent. Based on these results, we can conclude that the $g\text{-C}_3\text{N}_4\text{-CdS-CuO}$ composite was successfully used to develop a spPEC sensor for the detection of Hg^{2+} in human urine and artificial saliva.



Scheme 1. Schematic diagram of electrode preparation process (A) and schematic diagram of redox cycle on photoanode of self-powered device and test in actual sample (B).

2. Materials and Methods

2.1. Materials and Reagents

All chemicals (Table 1) were of analytical reagent grade, ultrapure water used in all solutions was from tap water purified by a Water Milli-Q system (Merck KGaA, Darmstadt, Germany). All instrumentations used in this work were listed in Table 2.

Table 1. Chemicals.

Chemicals	Manufacturer	Address
Melamine (C ₃ H ₆ N ₆ , 99.0%)	Macklin Co., Ltd.	Shanghai, China
Cadmium chloride hemi (pentahydrate) (CdCl ₂ ·2.5H ₂ O, 98.0%)	Macklin Co., Ltd.	Shanghai, China
Cupric oxide (CuO NPs, 99.5%)	Macklin Co., Ltd.	Shanghai, China
Sodium sulfide nonahydrate (Na ₂ S·9H ₂ O, 98.0%)	Xilong Scientific Co., Ltd.	Guangdong, China
Hydroxylammonium chloride (AR)	Cameo Chemical Reagent Co., Ltd.	Tianjin, China
Hydrochloric acid (HCl, AR)	Chuangdong Chemical Engineering Co., Ltd.	Chongqing, China
Sodium chloride (NaCl, 99.5%)	Jinshan Chemical Reagent Co., Ltd.	Chendu, China
Calcium chloride anhydrous (CaCl ₂ , 96.0%)	Sinopharm Chemical Reagent Co., Ltd.	Shanghai, China
Mucin	Sangong Bioengineering Co., Ltd.	Shanghai, China
Urea	Aladdin Industrial Co., Ltd.	Shanghai, China
Potassium bromate (KBrO ₃ , 99.9%)	Macklin Co., Ltd.	Shanghai, China
Potassium bromide (KBr, 99%)	Macklin Co., Ltd.	Shanghai, China
Sodium carbonate anhydrous (Na ₂ CO ₃ , 99.8%)	Yongda Chemical Reagent Co., Ltd.	Tianjin, China
Sodium hydrogen carbonate (NaHCO ₃ , 99.8%)	Yongda Chemical Reagent Co., Ltd.	Tianjin, China
Tris	Cameo chemical reagent Co., Ltd.	Tianjin, China
Nitric acid (HNO ₃ , 65.0–68.0%)	Chuangdong Chemical Engineering Co., Ltd.	Chongqing, China
Potassium chloride (KCl, 99.5%)	Jinshan Chemical Reagent Co., Ltd.	Chendu, China
Reduced glutathione (GSH, 98.0%)	Solarbio Science & Technology Co., Ltd.	Beijing, China
Glutathione reductase (GR, AR)	Solarbio Science & Technology Co., Ltd.	Beijing, China
Dihyronicotinamide-adenine dinucleotide phosphate, tetrasodium salt (NADPH, >98.0%)	Solarbio Science & Technology Co., Ltd.	Beijing, China
Sodium phosphate dibasic (Na ₂ HPO ₄ , 99.0%)	Cameo Chemical Reagent Co., Ltd.	Tianjin, China
Sodium dihydrogen phosphate (NaH ₂ PO ₄ , >99.0%)	Cameo Chemical Reagent Co., Ltd.	Tianjin, China
Potassium ferricyanide (K ₃ [Fe(CN) ₆], >99.5%)	Jinshan Chemical Reagent Co., Ltd.	Chendu, China
Potassium ferrocyanide (K ₄ [Fe(CN) ₆], >99.5%)	Jinshan Chemical Reagent Co., Ltd.	Chendu, China
Mercury chloride (HgCl ₂ , >99.5%)	Silver Lake Chemical Co., Ltd.	Guizhou, China

Table 2. Apparatus.

Apparatus	Model	Address
Electrochemical workstation	CHI660E	Shanghai Chenhua
Scanning electron microscopy (SEM)	Zeiss Sigma 300	Germany
Powder X-ray diffraction (XRD)	Bruker D8 Advance	Germany
UV-visible diffuse reflectance spectrum (UV-vis DRS)	Shimadzu UV-3600 Plus	Japan
Energy dispersive X-ray Spectroscopy (EDS)	Oxford Spectroscopy	Britain
Fourier transform infrared spectroscopy (FT-IR)	Perkin Elmer Spectrum Two FTIR-DTG	Britain

2.2. Photoelectrochemical Measurement

Prior to the photoelectrochemical measurement, g-C₃N₄ and CdS were prepared. The detailed preparation processes of these composites are illustrated in Support Information. Firstly, the bare FTO was cleaned ultrasonically in water, ethanol and acetone in sequence and dried at 60 °C. Then, 20 µL g-C₃N₄ suspension (1.0 mg mL⁻¹) was dropped on the FTO electrode with an active area of 0.25 cm² and dried at room temperature. After that, 20 µL CdS (5 mg mL⁻¹) and 20 µL CuO (1.0 mg mL⁻¹) were dropped on the FTO in the same operation, successively, to form layer upon layer of electrode materials. A three-electrode system was used to measure the photocurrent in CHI660E Electrochemical Workstation. The modified FTO was used as the working electrode, Pt wire as the counter electrode, and the saturated Ag/AgCl electrode as the reference electrode. GSH (15 mM, 1 mL), GR

(170 $\mu\text{g mL}^{-1}$, 2 μL) and NADPH (10 mg mL^{-1} , 250 μL) were added into the 0.1 M phosphate buffer solution (PBS) (5 mL, pH 7.4) as a redox cycle to realize signal amplification. The excitation light was turned on every 10 s in the photoelectric measurement process, and the voltage was constant at 0.0 V. The change in photocurrent was observed by adding different concentrations of mercury ions into the electrolyte.

2.3. Real Sample Processing

Urine samples [28]: 1 mL 50% hydrochloric acid and 0.8 mL 0.1 mol L^{-1} KBrO_3 /0.084 mol L^{-1} KBr were added to 10 mL urine samples; after reaction for 15 min, the appropriate amount of hydroxylamine (120 g L^{-1}) hydrochloride/sodium chloride (120 g L^{-1}) solution was added into the above mixture until the yellow color disappeared; samples were diluted to 50 mL with deionized water and diluted 10 times with PBS buffer before use.

Artificial saliva [29]: 0.6 mg mL^{-1} disodium hydrogen phosphate, 0.6 mg mL^{-1} anhydrous calcium chloride, 0.4 mg mL^{-1} potassium chloride, 0.4 mg mL^{-1} sodium chloride, 4 mg mL^{-1} mucin and 4 mg mL^{-1} urea was dissolved in 1 mL of the deionized water. This was set to pH 7.2, stored in the refrigerator and diluted 10 times with PBS buffer before use.

3. Results and Discussion

3.1. Characterizations of Composite Material

Scanning electron microscopy (SEM), X-ray diffraction (XRD), and Fourier transform infrared spectroscopy (FT-IR) were used to characterize the prepared composites and to analyze the electrode preparation process.

SEM images reveal that the bare FTO electrode is a uniform spongy layer (Figure 1A) [30]. After $\text{g-C}_3\text{N}_4$ is loaded onto FTO, the surface of the $\text{g-C}_3\text{N}_4$ /FTO electrode presents a typical plate-like structure (Figure 1B), which results from aggregation of the $\text{g-C}_3\text{N}_4$ sheets [31]. A large number of CdS QD nanoparticles are distributed on the surface of $\text{g-C}_3\text{N}_4$ (Figure 1C), which is consistent with the literature [32]. The large surface area of $\text{g-C}_3\text{N}_4$ serves as an effective anchor for loading CdS NPs. When the CdS QD- $\text{g-C}_3\text{N}_4$ /FTO electrode is covered with CuO nanoparticles (Figure 1D), the CuO nanoparticles appear to be nearly spherical [33]. SEM (Figure 1E,F) and elemental mapping by energy dispersive X-ray spectroscopy (Figure 1I) reveal that C, N, Cd, S, Cu, and O exist in the $\text{g-C}_3\text{N}_4$ -CdS-CuO electrode, indicating that the composite material is successfully loaded onto the FTO electrode.

The XRD analysis results of the crystal phase of the synthesized material are presented in Figure 1G. The XRD spectrum of $\text{g-C}_3\text{N}_4$ exhibits two evident diffraction peaks at 24.3° and 27.0° . These peaks represent the (100) and (002) planes of the graphite material, respectively, corresponding to the in-plane structure of the triazine ring and layered superposition of the conjugated aromatic groups [34]. The diffraction peaks of CdS at 26.5° , 37.6° , and 43.7° correspond to the (002), (102), and (103) crystal planes, respectively, which correlate with the wurtzite phase standard cards (JCPDS 80-0006) [35]. The diffraction peaks of the CuO nanoparticles at 35.6° , 38.7° , and 48.8° , in accordance with their monoclinic and crystalline nature, correspond to the (110), (111), and (200) crystal planes, respectively [33].

In the FT-IR spectra (Figure 1H) with the direct detection (Resolution: 4, Number of scans: 8, Detector: DTGS), $\text{g-C}_3\text{N}_4$ (curve a) exhibits strong absorption peaks in the range of $1200\text{--}1600\text{ cm}^{-1}$, which correspond to C-N heterocycles. The absorption band at 806 cm^{-1} corresponds to the typical breathing mode of the tri-s-triazine ring, and the intensity of the absorption peak near $2900\text{--}3400\text{ cm}^{-1}$ corresponds to the N-H stretching vibration [36]. The Cd-S band of CdS (curve b) demonstrates stretching and bending vibration absorption peaks at 631 cm^{-1} , whereas the peak at 1630 cm^{-1} corresponds to the O-H stretching vibrations [37]. For the CuO NPs (curve c), the peaks appearing at 701 cm^{-1} belong to the CuO NPs and confirm the formation of NPs [38]. Moreover, peaks corresponding to OH^- and C-O stretching vibrations can be observed from 2800 to 3600 cm^{-1} [39]. These results confirm that the composite and modified electrodes were successfully synthesized.

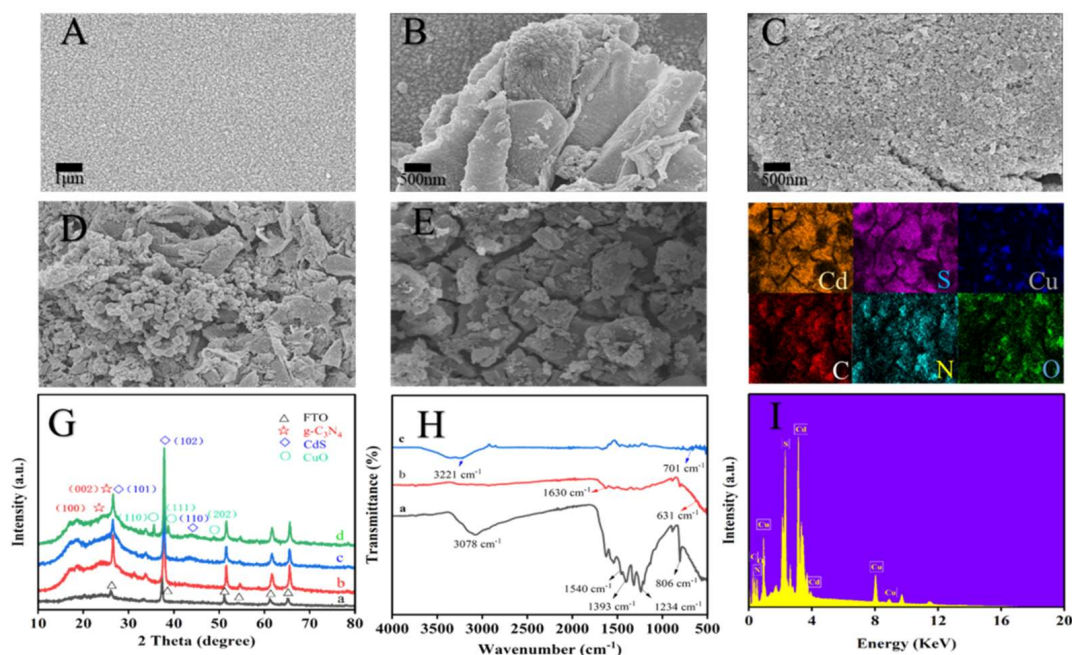


Figure 1. SEM images of naked FTO (A), $g\text{-C}_3\text{N}_4$ (B), CdS (C) and CuO (D); (E,F) SEM mapping image; XRD (G) includes a: FTO, b: $g\text{-C}_3\text{N}_4/\text{FTO}$, c: CdS- $g\text{-C}_3\text{N}_4/\text{FTO}$, d: CuO-CdS- $g\text{-C}_3\text{N}_4/\text{FTO}$; FT-IR (H) of a: $g\text{-C}_3\text{N}_4$, b: CdS and c: CuO; and (I) EDX spectrum of $g\text{-C}_3\text{N}_4\text{-CdS-CuO}$.

3.2. Electrochemical Activity of $g\text{-C}_3\text{N}_4\text{-CdS-CuO}$ Electrode

The electrochemical properties of the bare and material electrodes were studied, including the diffusion coefficient and heterogeneous electron-transfer rate constant. First, the electrochemical performances of the bare and modified electrodes were determined using cyclic voltammetry, in a 5 mM $[\text{Fe}(\text{CN})_6]^{3-/4-}$ solution containing 0.1 M KCl, by employing platinum as the counter electrode and saturated Ag/AgCl as the reference electrode (See supporting literature for details). As illustrated in Figure 2A,D, the current response increases gradually with an increase in the scanning rate and demonstrates a good linear relationship with the square root of the potential scanning rate, indicating that the redox reaction on the surface of the bare and modified electrodes is a diffusion control process. The electrically active area of the bare and $g\text{-C}_3\text{N}_4\text{-CdS-CuO}$ electrodes was calculated according to the Randles–Sevcik equation [40]: $I_p = 2.69 \times 10^5 \text{ A} \times n^{3/2} \times D^{1/2} \times C \times v^{1/2}$; where I_p denotes the maximum current (A), D denotes the diffusion coefficient (cm^2/s), $C = [\text{Fe}(\text{CN})_6]^{3-/4-}$ (mol/cm^3), n represents the number of transferred electrons, v denotes the scanning rate (V/s), and A indicates the effective working area (cm^2) of the modified electrode. The effective working area (A) can be calculated by a linear fitting of I_p to $v^{1/2}$. The active area of the bare electrode was 53.72 cm^2 (Figure 2B) and that of the $g\text{-C}_3\text{N}_4\text{-CdS-CuO}$ electrode was 72.40 cm^2 (Figure 2E). Thus, the larger the specific surface area of the $g\text{-C}_3\text{N}_4\text{-CdS-CuO}$ electrode, the more numerous the active sites are, and this is conducive to the amplification of electrical signals. In addition, the electron transfer rate constants of the bare and $g\text{-C}_3\text{N}_4\text{-CdS-CuO}$ electrodes can be calculated according to Nicholson's equation [41]: $\varphi = k_0[\pi D n F V / (RT)]^{-1/2}$; where φ denotes the peak-to-peak separation (δE_p), k_0 indicates the heterogeneous electron transfer rate constant, D represents the electroactive material diffusion coefficient, F denotes the Faraday constant, R represents the molar gas constant, and T denotes the temperature. The slope of the φ pair $[\pi D n F / (RT)]^{-1/2} v^{-1/2}$ curve corresponds to the heterogeneous electron transfer rate constant k_0 , which is $3.35 \times 10^{-4} \text{ cm s}^{-1}$ (Figure 2C) for the bare electrode and $2.72 \times 10^{-4} \text{ cm s}^{-1}$ (Figure 2F) for the $g\text{-C}_3\text{N}_4\text{-CdS-CuO}$ electrode. This indicates that the electrochemical equilibrium time required by the $g\text{-C}_3\text{N}_4\text{-CdS-CuO}$ -modified electrode was not significantly shortened.

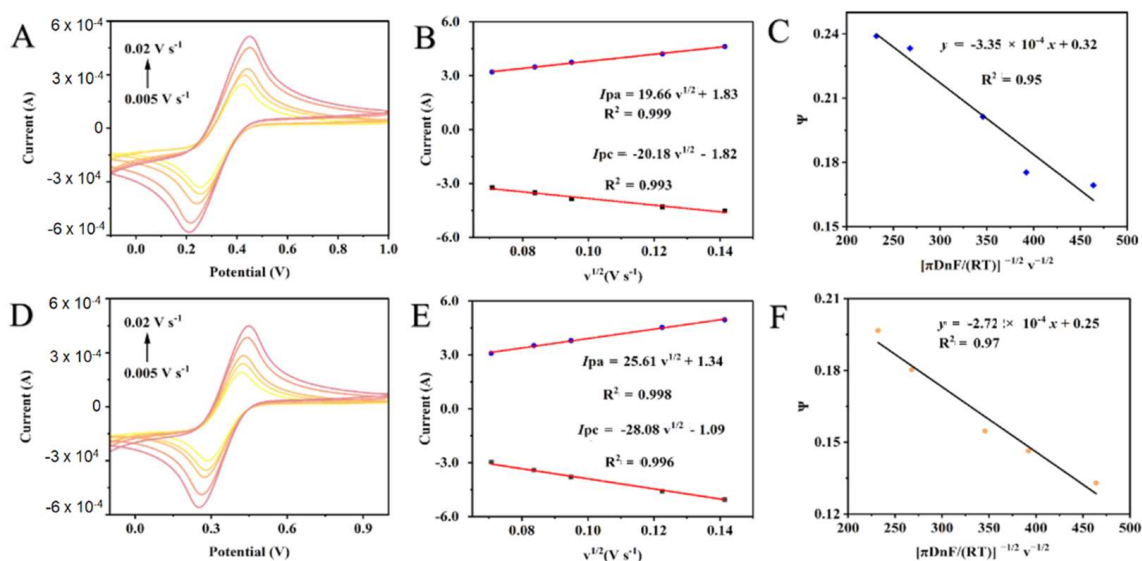


Figure 2. The cyclic voltammetry (CV) curves of the bare electrode (A) and the g-C₃N₄-CdS-CuO modified electrodes (D) at different scan rates (0.005~0.02 V/s), and bare electrode (B) and the g-C₃N₄-CdS-CuO modified electrodes (E) of linear relationship between the anodic and cathodic peak currents versus the square of the root of the scan rate, the plots of ϕ values vs. $[\pi DnF/(RT)]^{-1/2} v^{-1/2}$: (C) the bare electrode and (F) the g-C₃N₄-CdS-CuO modified electrodes.

3.3. Feasibility of the Designed Strategy

To evaluate the spPEC properties of the fabricated CuO-CdS-g-C₃N₄/FTO electrode, photocurrent responses of bare FTO, g-C₃N₄/FTO, CdS-g-C₃N₄/FTO, and CuO-CdS-g-C₃N₄/FTO were monitored (Figure 3A). The photocurrent of CuO-CdS-g-C₃N₄/FTO (column c) is better than that of g-C₃N₄/FTO (column a) and CuO-CdS-g-C₃N₄/FTO (column b), which is further verified by electronic impedance spectroscopy (EIS), recorded by the EIS different changes of preparing the electrodes in ferricyanide/ferrocyanide mixed solution ($[\text{Fe}(\text{CN})_6]^{3-/4-}$) (See supporting literature for details). As illustrated in Figure 3B, the resistance of g-C₃N₄/FTO (curve b) is larger than that of FTO (curve a), which may be attributed to the poor conductivity of g-C₃N₄/FTO. The resistance of CdS-g-C₃N₄/FTO (curve c) is lower than that of FTO, indicating that CdS promotes g-C₃N₄ electron transfer. Moreover, the resistance of CuO-CdS-g-C₃N₄/FTO (curve d) is less than that of CdS-g-C₃N₄/FTO, which indicates that CuO increases the transfer of electrode current and further increases the photocurrent. The feasibility analysis further verifies this principle.

To verify the amplification caused by the redox cycle strategy, the developed spPEC sensor was studied using the photocurrent output. For comparison, we also carried out the comparison experiment of redox single signal amplification and double signal amplification; that is, under the same conditions, different concentrations of Hg²⁺ (0.5 nM, 10 nM) were added to GSH (Figure 3C) and GSH, NADPH, and GR (Figure 3D) solutions respectively. As presented in Figure 3C, GSH is oxidized by CuO to GSSG to generate a strong photocurrent (column b vs. a) and single signal amplification was achieved. When Hg²⁺ was added from 0.5 nM to 10 nM, the photocurrent ΔI increased from 0.97 μA to 2.27 μA (column c and d). These results demonstrate that the GSH could specifically recognize Hg²⁺, and the photocurrent was inversely proportional to the concentration of Hg²⁺. Evidently, when NADPH and GR are added (Figure 3D), the photocurrent reaches a maximum (column b vs. a) and double signal amplification. In the presence of GR, GSSG is reduced to GSH using NADPH as a substrate, thereby resulting in a self-powered redox cycle system. When Hg²⁺ was added from 0.5 nM to 10 nM, the photocurrent ΔI increased from 2.49 μA to 3.59 μA (columns c and d), which was the same as the photocurrent trend in Figure 3C, indicating that both methods were beneficial to PEC detection, and the detection effect of

double signal amplification was better. Therefore, the GSH-NADPH-GR redox cycle can be used as a signal amplification strategy to improve the detection sensitivity for Hg^{2+} .

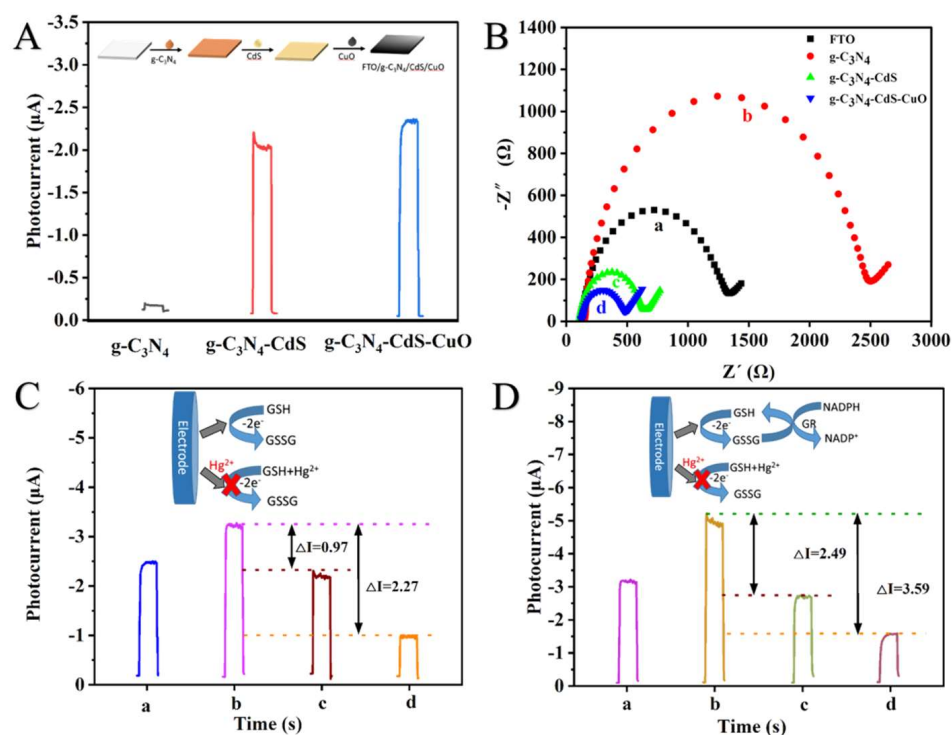
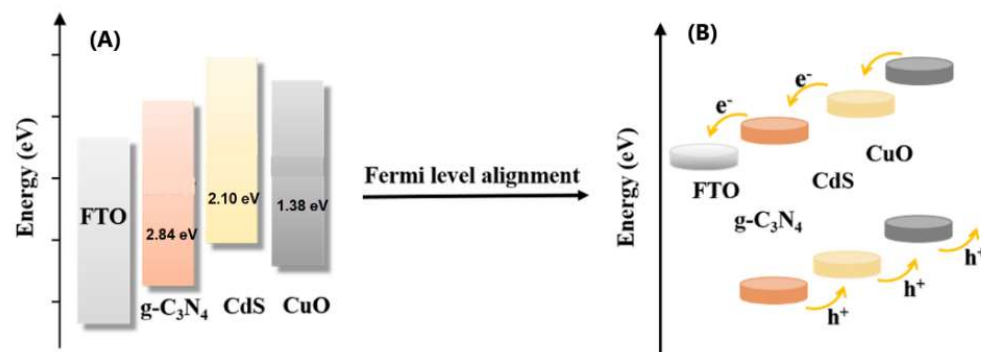


Figure 3. PEC responses of the FTO electrode in PBS buffer solutions containing: $g\text{-C}_3\text{N}_4/\text{FTO}$; $\text{CdS-}g\text{-C}_3\text{N}_4/\text{FTO}$; $\text{CuO-CdS-}g\text{-C}_3\text{N}_4/\text{FTO}$ (A); and EIS of the electrode, a, bare FTO; b, $g\text{-C}_3\text{N}_4/\text{FTO}$; c, $\text{CdS-}g\text{-C}_3\text{N}_4/\text{FTO}$; d, $\text{CuO-CdS-}g\text{-C}_3\text{N}_4/\text{FTO}$ (B). The photocurrent response of a, $\text{CuO-CdS-}g\text{-C}_3\text{N}_4/\text{FTO}$; b, $\text{CuO-CdS-}g\text{-C}_3\text{N}_4/\text{FTO} + \text{GSH}$; c, $\text{CuO-CdS-}g\text{-C}_3\text{N}_4/\text{FTO} + \text{GSH} + 0.5 \text{ nM Hg}^{2+}$; d, $g\text{-C}_3\text{N}_4\text{-CdS-CuO} + \text{GSH} + 10 \text{ nM Hg}^{2+}$ (C); and the photocurrent response of a, $\text{CuO-CdS-}g\text{-C}_3\text{N}_4/\text{FTO} + \text{GSH}$; b, $\text{CuO-CdS-}g\text{-C}_3\text{N}_4/\text{FTO} + \text{GSH} + \text{NADPH} + \text{GR}$; c, $\text{CuO-CdS-}g\text{-C}_3\text{N}_4/\text{FTO} + \text{GSH} + \text{NADPH} + \text{GR} + 0.5 \text{ nM Hg}^{2+}$; d, $\text{CuO-CdS-}g\text{-C}_3\text{N}_4/\text{FTO} + \text{GSH} + \text{NADPH} + \text{GR} + 10 \text{ nM Hg}^{2+}$ (D).

Ultraviolet–visible diffuse reflection spectroscopy (DRS) was used to study the electronic orientation of the composite materials. The band gap of the three semiconductors was calculated according to the equation $(\alpha h\nu)^2 = C(h\nu - E_g)$ (where α , $h\nu$, C , and E_g are the absorption coefficient, photoenergy, the constant, and band gap energy, respectively) [42] and extrapolated the intercept of the linear part of $(\alpha h\nu)^2$ vs. $h\nu$ plot to the x -axis shown in Figure S1A. The band gaps (E_g) of $g\text{-C}_3\text{N}_4$, CdS, and CuO are 2.84 eV, 2.10 eV, and 1.38 eV, respectively. The conduction bands (E_{CB}) and valence bands (E_{VB}) were estimated using the following formula: $E_{\text{CB}} = X - E_c - E_g/2$ ($E_c = 4.5 \text{ eV}$) and $E_{\text{VB}} = E_{\text{CB}} + E_g$, where X and E_g denote the geometric average value of the absolute electronegativity of each atom in the semiconductor and the band gap width of the semiconductor, respectively. The E_{CB} values of $g\text{-C}_3\text{N}_4$, CdS, and CuO were 0.92 eV, -0.36 eV , and 0.62 eV, respectively, and the E_{VB} values of $g\text{-C}_3\text{N}_4$, CdS, and CuO were 3.76 eV, 1.74 eV, and 2.0 eV, respectively. The band gaps of $g\text{-C}_3\text{N}_4$, CdS, and CuO reported in the literature are presented in Scheme 2A [43]. When $g\text{-C}_3\text{N}_4$, CdS, and CuO are in contact, the energy level differences between CdS and $g\text{-C}_3\text{N}_4$ and between CdS and CuO (Fermi–Dirac statistics) cause electrons to flow from CdS (high energy level) to $g\text{-C}_3\text{N}_4$ and CuO (low energy level). If the material is described in terms of a Fermi–Dirac distribution, this electron transfer is referred to as a Fermi level alignment. The redistribution of electrons between CdS and $g\text{-C}_3\text{N}_4$ and between CdS and CuO is assumed to trigger the downward and upward movement of CdS, $g\text{-C}_3\text{N}_4$ and CuO band edges, respectively. Therefore, we can infer that the electron orientation of the $g\text{-C}_3\text{N}_4\text{-CdS-CuO}$ electrode demonstrates a stepped structure, as illustrated in Scheme 2B.

The edges of the conduction and valence bands of these three materials increased in the following order: $g\text{-C}_3\text{N}_4 < \text{CdS} < \text{CuO}$; that is, the CdS layer was inserted between $g\text{-C}_3\text{N}_4$ and CuO to increase the conduction band edge of CuO, providing a higher driving force for the injection of excited-state electrons from outside the CuO layer. When $g\text{-C}_3\text{N}_4\text{-CdS-CuO}$ was photoexcited under irradiation, the stepped structure at the edge of the band proved not only beneficial for electron injection in $g\text{-C}_3\text{N}_4\text{-CdS-CuO}$, but also for hole recovery. Under irradiation, the $g\text{-C}_3\text{N}_4\text{-CdS-CuO}$ material generated a photocurrent, and the GSH-NADPH-GR redox cycle acted as a self-powered system to further increase the photocurrent and achieve signal amplification (Figure S1B).



Scheme 2. Band gap of $g\text{-C}_3\text{N}_4$, CdS, and CuO nanomaterial (A), Band structure of electrode after electron redistribution between $g\text{-C}_3\text{N}_4$, CdS, and CuO interface (Fermi-level arrangement) (B).

3.4. Optimization of Experimental Conditions

To improve the sensitivity of the sensor, we optimized the experimental parameters by using the photocurrent of PEC. We primarily optimized the concentration of NADPH (Figure S2A), and a maximum change was noted when the amount of NADPH was $0.40 \mu\text{g}/\mu\text{L}$ ($250 \mu\text{L}$). The amount of GR was also optimized, which is one of the most important factors in the signal detection process. As illustrated in Figure S2B, when different concentrations of GR are added to the bath solution, a maximum photocurrent signal can be obtained at $2.08 \text{ ng}/\mu\text{L}$ ($2 \mu\text{L}$). Next, we determined the optimal GSH concentration (Figure S2C). The maximum signal was obtained at a concentration of 15 mM, after which the signal slowly diminished. Thus, 15 mM was selected as the optimal concentration for GSH. Finally, we optimized the mass ratio of $g\text{-C}_3\text{N}_4$ to CuO. As presented in Figure S2D, the photocurrent signal of the material reaches a maximum when the ratio of $g\text{-C}_3\text{N}_4$ and CuO is 1:1. As shown in Figure S2E, when using a $\text{Na}_2\text{CO}_3\text{-NaHCO}_3$ (0.1 M, pH 7.4) and tris- HNO_3 (0.1 M, pH 7.4) buffer, the signal response of the photocurrent decreases. In contrast, no corresponding interference can be observed in PBS (0.1 M, pH 7.4). Therefore, we think that using PBS (0.1 M, pH 7.4) to prepare the bath solution will result in a better signal response.

3.5. Analytical Performance and Selectivity and Stability

To verify the analytical performance of the proposed spPEC sensing system, different concentrations of Hg^{2+} were added and measured under the optimal conditions. As illustrated in Figure 4A, the photocurrent signal gradually weakens with increasing Hg^{2+} concentration. Hg^{2+} is linearly and logarithmically correlated in the range between 5 pM and 100 nM. The regression equation was $Y = 0.90 \text{Log}C_{\text{Hg}^{2+}} - 2.40$ ($R^2 = 0.993$), and the calculation formula for detection limit is $S/N = 3$ [44]. The detection limit was 0.84 pM (Figure 4B). Compared with other Hg^{2+} detection methods, this sensor demonstrated a picomolar detection sensitivity for Hg^{2+} without requiring aptamer fixing and pretreatment processes (Table S1). Therefore, we can conclude that the detection efficiency of the sensor is significantly improved.

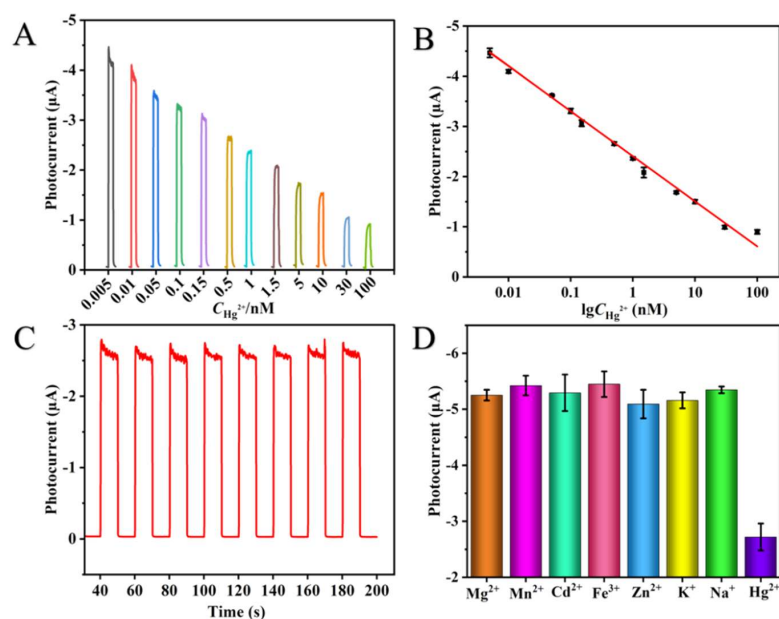


Figure 4. (A) PEC reaction of Hg²⁺ at different concentrations; (B) Linear relationship between photocurrent and logarithm value of Hg²⁺ concentration; (C) Sensor stability within 200 s; (D) Selectivity of PEC system.

The experimental results indicated that the PEC response did not change significantly within 200 s (Figure 4C), and the relative standard deviation (RSD) of the PEC response change was less than 0.77%. To assess the selectivity of the constructed spPEC sensor, we investigated its specificity for Hg²⁺ (0.5 nM). Among several analogs, including Mg²⁺, Mn²⁺, Cd²⁺, Fe³⁺, Zn²⁺, K⁺, and Na⁺ (50 nM), a much lower current value was recorded with Hg²⁺ than with other interfering species (Figure 4D). This result demonstrates the excellent selectivity of the spPEC method for Hg²⁺. The stability of the sensor was also evaluated for the detection of 0.5 nM Hg²⁺. Moreover, to evaluate the repeatability of the proposed sensor, six replicate measurements were performed with the sensor using 0.5 nM Hg²⁺ (Figure S3). The results revealed an RSD of 0.53%, indicating reasonable repeatability of the spPEC sensor for Hg²⁺ detection.

3.6. Analysis of Real Samples

To investigate whether the proposed method could be used to detect Hg²⁺ in complex samples, the experiment was conducted for two different substances (the urine of healthy people and artificial saliva). The standard addition method was used to evaluate the feasibility of the method for actual samples, as presented in Table 3. The concentration of Hg²⁺ was in the range 0.1–10 nM, and the recovery rate was between 93.56% and 103.02%, indicating possible applicability of the spPEC sensor for detecting Hg²⁺ in real-sample application.

Table 3. Comparison of Hg²⁺ determination in human urine samples and artificial saliva.

Sample	Applied (nM)	Found (nM)	Recovery (%)	RSD (%)
Urine	0	-	-	1.76
	0.1	0.09	97.14	2.03
	1	0.98	98.81	2.74
	10	10.3	103.02	2.19
Saliva	0	-	-	2.71
	0.1	0.09	93.56	2.88
	1	0.97	97.97	2.33
	10	9.92	99.24	3.07

"-" Indicates that it is below detection limit.

4. Conclusions

A new spPEC sensor for Hg^{2+} detection based on g- C_3N_4 -CdS-CuO composites, as well as a redox-cycle signal-amplification strategy were developed. The novel g- C_3N_4 -CdS-CuO co-sensitized modified electrode, which exhibits large surface area and improved photoelectric response due to a cascade structure, was successfully used to detect target ions in complex samples. In addition, the self-powered sensor demonstrated satisfactory sensitivity owing to double signal amplification (GSH and GSH-NADPH-GR) and a limit of detection of 0.84 pM for Hg^{2+} . More importantly, in vitro application of the GSH-NADPH-GR redox cycle demonstrated its potential as a photoelectrochemical sensor and, therefore, presented a new method for constructing novel sensors. The sensor also demonstrated significant potential for detecting Hg^{2+} in human urine and artificial saliva samples. More significantly, the developed approach can also be used to detect other heavy metal ions according to the HSAB theory and may serve as a new analytical tool for specific, sensitive, and reliable analysis of heavy metal ions in clinical toxicology, food, and the environment.

Supplementary Materials: The following supporting information can be downloaded at: <https://www.mdpi.com/article/10.3390/chemosensors10070286/s1>, Figure S1: The band gaps of g- C_3N_4 , CdS, and CuO were measured by the UV-vis diffuse reflection spectra (DRS) (A), the picture shows the direction of electrons in the photoelectric sensor under light conditions (B); Figure S2: (A) Concentration of NADPH; (B) Concentration of GR; (C) Concentration of GSH; (D) Mass ratio of g- C_3N_4 to CuO; (E) Different types of buffer solutions (0.1M); Figure S3: Reproducibility of g- C_3N_4 -CdS-CuO at 0.5 nM Hg^{2+} ; Table S1: Comparison of other analysis strategies for Hg^{2+} detection. References [10,25,34,45–50] are cited in the supplementary materials.

Author Contributions: Conceptualization, B.L. and Y.L.; methodology, Y.S.; validation, Y.S.; formal analysis, L.S.; investigation, L.S.; data curation, Y.S.; writing—original draft preparation, Y.S.; writing—review and editing, D.T. and B.L.; supervision, D.T. and B.L.; funding acquisition, B.L. All authors have read and agreed to the published version of the manuscript.

Funding: This research was funded by the National Natural Science Foundation of China (21864007, 21904056, 21605029), and Guizhou Provincial Natural Science Foundation (Qian Ke He Ji Chu [2020]1Y042, [2017]5788 Qian Ke He Platform for Talents, [2018]5781 Qian Ke He Platform for Talents).

Institutional Review Board Statement: Not applicable.

Informed Consent Statement: Not applicable.

Data Availability Statement: The data presented in this study are available on request from the corresponding author.

Conflicts of Interest: The authors declare no conflict of interest.

References

1. Al-Saleh, I. Potential health consequences of applying mercury-containing skin-lightening creams during pregnancy and lactation periods. *Int. J. Hyg. Environ. Health* **2016**, *219*, 468–474. [[CrossRef](#)] [[PubMed](#)]
2. Liu, J.; Tai, W.J.; Wang, D.L.; Liu, J.; Su, J.; Yu, L. Cholesteric liquid crystal photonic hydrogel films immobilized with urease used for the detection of Hg^{2+} . *Chemosensors* **2022**, *10*, 140. [[CrossRef](#)]
3. Shellaiah, M.; Sun, K. Progress in metal-organic frameworks facilitated mercury detection and removal. *Chemosensors* **2021**, *9*, 101. [[CrossRef](#)]
4. Lian, Q.; Liu, H.; Zheng, X.F.; Li, X.M.; Zhang, F.J.; Gao, J. Enhanced peroxidase-like activity of CuO/Pt nanoflowers for colorimetric and ultrasensitive Hg^{2+} detection in water sample. *Appl. Surf. Sci.* **2019**, *483*, 551–561. [[CrossRef](#)]
5. Lu, L.L.; Han, X.; Lin, J.W.; Zhang, Y.X.; Qiu, M.H.; Chen, Y.; Li, M.J.; Tang, D.P. Ultrasensitive fluorometric biosensor based on Ti_3C_2 MXenes with Hg^{2+} -triggered exonuclease III-assisted recycling amplification. *Analyst* **2021**, *146*, 2664–2669. [[CrossRef](#)]
6. Wu, Y.; Jiang, T.T.; Wu, Z.Y.; Yu, R.Q. Novel ratiometric surface-enhanced Raman spectroscopy aptasensor for sensitive and reproducible sensing of Hg^{2+} . *Biosens. Bioelectron.* **2018**, *99*, 646–652. [[CrossRef](#)]
7. Chang, Y.Y.; Tang, X.L.; Huang, J.Q.; Chai, Y.Q.; Zhuo, Y.; Li, H.; Yuan, R. Programming a “crab claw”-like DNA nanomachine as a super signal amplifier for ultrasensitive electrochemical assay of Hg^{2+} . *Anal. Chem.* **2021**, *93*, 12075–12080. [[CrossRef](#)]
8. Hisham, A.; Alexei, N.; Thomas, J.S. Development of novel and highly specific ssDNA-aptamer-based electrochemical biosensor for rapid detection of mercury (II) and lead (II) Ions in Water. *Chemosensors* **2019**, *7*, 27. [[CrossRef](#)]

9. Wang, D.; Gai, Q.; Huang, R.; Zheng, X. Label-free electrochemiluminescence assay for aqueous Hg^{2+} through oligonucleotide mediated assembly of gold nanoparticles. *Biosens. Bioelectron.* **2017**, *98*, 134–139. [[CrossRef](#)]
10. Singh, S.; Numan, A.; Zhan, Y.Q.; Singh, V.; Hung, T.V.; Nam, N.D. A novel highly efficient and ultrasensitive electrochemical detection of toxic mercury (II) ions in canned tuna fish and tap water based on a copper metal-organic framework. *J. Hazard. Mater.* **2020**, *399*, 123042. [[CrossRef](#)]
11. Shu, J.; Tang, D.P. Recent advances in photoelectrochemical sensing: From engineered photoactive materials to sensing devices and detection modes. *Anal. Chem.* **2020**, *92*, 363–377. [[CrossRef](#)] [[PubMed](#)]
12. Yu, Z.C.; Xu, J.H.; Gong, H.X.; Li, Y.X.; Li, L.; Wei, Q.H.; Tang, D.P. Bioinspired self-powered piezoresistive sensor for simultaneous monitoring of human health and outdoor UV light intensity. *ACS Appl. Mater. Interfaces* **2022**, *14*, 5101–5111. [[CrossRef](#)] [[PubMed](#)]
13. Yu, Z.C.; Gong, H.X.; Li, Y.X.; Xu, J.H.; Zhang, J.; Zeng, Y.Y.; Liu, X.L.; Tang, D.P. Chemiluminescence-derived self-powered photoelectrochemical immunoassay for detecting low-abundance disease-related protein. *Anal. Chem.* **2021**, *93*, 13389–13397. [[CrossRef](#)] [[PubMed](#)]
14. Peng, B.; Zhang, Z.L.; Tang, L.; Ouyang, X.L.; Zhu, X.; Chen, L.; Fan, X.Y.; Zhou, Z.P.; Wang, J.J. Self-powered photoelectrochemical aptasensor for oxytetracycline cathodic detection based on a dual Z-scheme $\text{WO}_3/\text{g-C}_3\text{N}_4/\text{MnO}_2$ photoanode. *Anal. Chem.* **2021**, *93*, 9129–9138. [[CrossRef](#)]
15. Cao, J.T.; Lv, J.L.; Liao, X.J.; Ma, S.H.; Liu, Y.M. A membraneless self-powered photoelectrochemical biosensor based on $\text{Bi}_2\text{S}_3/\text{BiPO}_4$ heterojunction photoanode coupling with redox cycling signal amplification strategy. *Biosens. Bioelectron.* **2022**, *195*, 113651. [[CrossRef](#)] [[PubMed](#)]
16. Zhang, K.Y.; Lv, S.Z.; Zhou, Q.; Tang, D.P. CoOOH nanosheets-coated $\text{g-C}_3\text{N}_4/\text{CuInS}_2$ nanohybrids for photoelectrochemical biosensor of carcinoembryonic antigen coupling hybridization chain reaction with etching reaction. *Sens. Actuators B* **2020**, *307*, 127631. [[CrossRef](#)]
17. Duan, W.; Yan, P.C.; Dong, J.T.; Chen, Y.; He, X.Y.; Chen, J.P.; Qian, J.C.; Xu, L.; Li, H.N. A self-powered photoelectrochemical aptamer probe for oxytetracycline based on the use of a NiO nanocrystal/ $\text{g-C}_3\text{N}_4$ heterojunction. *Microchim. Acta* **2019**, *186*, 737. [[CrossRef](#)]
18. Zeng, R.J.; Luo, Z.B.; Su, L.S.; Zhang, L.J.; Tang, D.P.; Niessner, R.; Knopp, D. Palindromic molecular beacon-based Z-scheme BiOCl-Au-CdS photoelectrochemical biodetection. *Anal. Chem.* **2019**, *91*, 2447–2454. [[CrossRef](#)]
19. Liu, Y.X.; Ma, H.M.; Zhang, Y.; Pang, X.H.; Fan, D.W.; Wu, D.; Wei, Q. Visible light photoelectrochemical aptasensor for adenosine detection based on $\text{CdS/PPy/g-C}_3\text{N}_4$ nanocomposites. *Biosens. Bioelectron.* **2016**, *86*, 439–445. [[CrossRef](#)]
20. Luo, Z.B.; Zhang, L.J.; Zeng, R.J.; Su, L.S.; Tang, D.P. Near-infrared light-excited core-core-shell UCNP@Au@CdS upconversion nanospheres for ultrasensitive photoelectrochemical enzyme immunoassay. *Anal. Chem.* **2018**, *90*, 9568–9575. [[CrossRef](#)]
21. Li, X.M.; Kong, W.S.; Qin, X.; Qu, F.L.; Lu, L.M. Self-powered cathodic photoelectrochemical aptasensor based on in situ-synthesized $\text{CuO-Cu}_2\text{O}$ nanowire array for detecting prostate-specific antigen. *Microchim. Acta* **2020**, *187*, 325. [[CrossRef](#)] [[PubMed](#)]
22. Zhao, L.L.; Chen, Y.R.; Wu, X.M.; Li, Z.J.; Dong, Y.M.; Wang, G.L. Invoking cathodic photoelectrochemistry through a spontaneously coordinated electron transporter: A proof of concept toward signal transduction for bioanalysis. *Anal. Chem.* **2021**, *93*, 17119–17126. [[CrossRef](#)]
23. Senobari, S.; Nezamzadeh-Ejehieh, A. A comprehensive study on the photocatalytic activity of coupled copper oxide-cadmium sulfide nanoparticles. *Spectrochim. Acta Part A* **2018**, *196*, 334–343. [[CrossRef](#)] [[PubMed](#)]
24. He, L.Y.; Lu, Y.X.; Gao, X.Y.; Song, P.S.; Huang, Z.X.; Liu, S.; Liu, Y.Y. Self-cascade system based on cupric oxide nanoparticles as dual-functional enzyme mimics for ultrasensitive detection of silver ions. *ACS Sustain. Chem. Eng.* **2018**, *6*, 12132–12139. [[CrossRef](#)]
25. Zhang, X.Y.; Li, M.Y.; He, L.M.; Tian, D.D.; Zhang, L.J.; Zhang, J.H.; Liu, M. Highly sensitive and selective photoelectrochemical sensor for mercury (II) detection based on efficient Bi_2MoO_6 photoanode decorated with CuS. *J. Alloys Compd.* **2020**, *864*, 157905. [[CrossRef](#)]
26. Moreno-Sánchez, R.; Marín-Hernández, Á.; Gallardo-Pérez, J.C.; Vázquez, C.; Rodríguez-Enríquez, S.; Saavedra, E. Control of the NADPH supply and GSH recycling for oxidative stress management in hepatoma and liver mitochondria. *BBA-Bioenerg.* **2018**, *1859*, 1138–1150. [[CrossRef](#)]
27. Pang, X.L.; Bai, H.Y.; Zhao, H.Q.; Liu, Y.C.; Qin, F.Y.; Han, X.; Fan, W.Q.; Shi, W.D. Biothiol-functionalized cuprous oxide Sensor for dual-mode sensitive Hg^{2+} detection. *ACS Appl. Mater. Interfaces* **2021**, *13*, 46980–46989. [[CrossRef](#)]
28. She, P.; Chu, Y.X.; Liu, C.W.; Guo, X.; Zhao, K.; Li, J.G.; Du, H.J.; Zhang, X.; Wang, H.; Deng, A.P. A competitive immunoassay for ultrasensitive detection of Hg^{2+} in water, human serum and urine samples using immunochromatographic test based on surface-enhanced Raman scattering. *Anal. Chim. Acta* **2016**, *906*, 139–147. [[CrossRef](#)]
29. Wordofa, D.N.; Ramnani, P.; Tran, T.; Mulchandani, A. An oligonucleotide-functionalized carbon nanotube chemiresistor for sensitive detection of mercury in saliva. *Analyst* **2016**, *141*, 2756–2760. [[CrossRef](#)]
30. Saghi, E.; Rounaghi, G.H.; Sarafraz-Yazdi, A.; Razavipanah, I.; Moosavi, P.M. Fluorine-tin oxide (FTO) electrode modified with platinum nanoparticles dispersed into montmorillonite clay as an effective and low-cost catalyst for ethanol electrooxidation. *RSC Adv.* **2016**, *6*, 113240–113248. [[CrossRef](#)]
31. Li, R.Z.; Liu, Y.; Cheng, L.; Yang, C.Z.; Zhang, J.D. Photoelectrochemical Aptasensing of Kanamycin Using Visible Light-Activated Carbon Nitride and Graphene Oxide Nanocomposites. *Anal. Chem.* **2014**, *86*, 9372–9375. [[CrossRef](#)] [[PubMed](#)]

32. Liu, Y.; Yan, K.; Zhang, J.D. Graphitic carbon nitride sensitized with CdS quantum dots for visible-light-driven photoelectrochemical aptasensing of tetracycline. *ACS Appl. Mater. Interfaces* **2016**, *8*, 28255–28264. [[CrossRef](#)] [[PubMed](#)]
33. Alsamhary, K.; Al-Enazi, N.M.; Alhomaidi, E.; Alwakeel, S. Spirulina platensis mediated biosynthesis of CuO Nps and photocatalytic degradation of toxic azo dye Congo red and kinetic studies. *Environ. Res.* **2021**, *207*, 112172. [[CrossRef](#)]
34. Li, Z.P.; Dong, W.X.; Du, X.Y.; Wen, G.G.; Fan, X.J. A novel photoelectrochemical sensor based on g-C₃N₄@CdS QDs for sensitive detection of Hg²⁺. *Microchem. J.* **2020**, *152*, 104259. [[CrossRef](#)]
35. Yu, Z.G.; Huang, L.T.; Chen, J.L.; Li, M.J.; Tang, D.P. Graded oxygen-doped CdS electrode for portable photoelectrochemical immunoassay of alpha-fetoprotein coupling with a digital multimeter readout. *Sens. Actuators B* **2021**, *343*, 130136. [[CrossRef](#)]
36. Ouyang, X.L.; Feng, C.Y.; Tang, L.; Zhu, X.; Peng, B.; Fan, X.Y.; Liao, Y.B.; Zhou, Z.P.; Zhang, Z.L. A flexible photoelectrochemical aptasensor using heterojunction architecture of α -Fe₂O₃/d-C₃N₄ for ultrasensitive detection of penbritin. *Biosens. Bioelectron.* **2022**, *197*, 113734. [[CrossRef](#)] [[PubMed](#)]
37. Zhang, K.Y.; Lv, S.Z.; Lin, Z.Z.; Tang, D.P. CdS:Mn quantum dot-functionalized g-C₃N₄ nanohybrids as signal-generation tags for photoelectrochemical immunoassay of prostate specific antigen coupling DNAzyme concatamer with enzymatic biocatalytic precipitation. *Biosens. Bioelectron.* **2017**, *95*, 34–40. [[CrossRef](#)]
38. Ali, K.; Ahmed, B.; Ansari, S.M.; Saquib, Q.; Al-Khedhairi, A.A.; Dwivedi, S.; Alshaeri, M.; Khan, M.S.; Musarrat, J. Comparative in situ ROS mediated killing of bacteria with bulk analogue, eucalyptus leaf extract (ELE)-capped and bare surface copper oxide nanoparticles. *Mater. Sci. Eng. C* **2019**, *100*, 747–758. [[CrossRef](#)]
39. Anwaar, S.; Maqbool, Q.; Jabeen, N.; Nazar, M.; Abbas, F.; Nawaz, B.; Hussain, T.; Hussain, S.Z. The effect of green synthesized CuO nanoparticles on callogenesis and regeneration of *Oryza sativa*. *Front. Plant Sci.* **2016**, *7*, 1330. [[CrossRef](#)]
40. Lv, Z.J.; Zhu, L.; Yin, Z.P.; Li, M.J.; Tang, D.P. Signal-on photoelectrochemical immunoassay mediated by the etching reaction of oxygen/phosphorus co-doped g-C₃N₄/AgBr/MnO₂ nanohybrids. *Anal. Chim. Acta* **2021**, *1171*, 338680. [[CrossRef](#)]
41. Gaillard, M.; Kanso, H.; Denat, F.; Calas-Blanchard, C.; Inguibert, N.; Noguier, T. Fe (III)-DOTA/ Fe (III)-NOTA complexes: Attractive alternative markers for future electrochemical biosensors. *J. Electrochem. Soc.* **2020**, *167*, 117502. [[CrossRef](#)]
42. Luo, D.J.; Fu, Q.P.; Gao, R.; Su, L.X.; Su, Y.H.; Liu, B.Q. Signal-on photoelectrochemical immunoassay for salivary cortisol based on silver nanoclusters-triggered ion-exchange reaction with CdS quantum dots. *Anal. Bioanal. Chem.* **2022**, *414*, 3033–3042. [[CrossRef](#)]
43. Lee, Y.L.; Lo, Y.S. Highly Efficient quantum-dot-sensitized solar cell based on Co-sensitization of CdS/CdSe. *Adv. Funct. Mater.* **2009**, *19*, 604–609. [[CrossRef](#)]
44. Luo, D.J.; Liu, B.Q.; Gao, R.; Su, L.X.; Su, Y.H. TiO₂/CuInS₂-sensitized structure for sensitive photoelectrochemical immunoassay of cortisol in saliva. *J. Solid State Electrochem.* **2022**, *26*, 749–759. [[CrossRef](#)]
45. Dong, Y.X.; Cao, J.T.; Wang, B.; Ma, S.H.; Liu, Y.M. Spatial-Resolved Photoelectrochemical Biosensing Array Based on a CdS@g-C₃N₄ Heterojunction: A Universal Immunosensing Platform for Accurate Detection. *ACS Appl. Mater. Interfaces* **2018**, *10*, 3723–3731. [[CrossRef](#)] [[PubMed](#)]
46. Zhang, Y.H.; Li, M.J.; Wang, H.J.; Yuan, R.; Wei, S.P. Supersensitive Photoelectrochemical Aptasensor Based on Br,N-Codoped TiO₂ Sensitized by Quantum Dots. *Anal. Chem.* **2019**, *91*, 10864–10869. [[CrossRef](#)]
47. Zhang, K.Y.; Sang, Y.X.; Gao, Y.D.; Sun, Q.X.; Li, W.N. A fluorescence turn-on CDs-AgNPs composites for highly sensitive and selective detection of Hg²⁺. *Spectrochim. Acta Part A* **2022**, *264*, 120281. [[CrossRef](#)]
48. Li, D.W.; Ling, S.; Cheng, X.R.; Yang, Z.Q.; Lv, B. Development of a DNAzyme-based colorimetric biosensor assay for dual detection of Cd²⁺ and Hg²⁺. *Anal. Bioanal. Chem.* **2021**, *413*, 7081–7091. [[CrossRef](#)]
49. Ran, Q.X.; Sheng, F.F.; Chang, G.R.; Zhong, M.; Xu, S.X. Sulfur-doped reduced graphene oxide@chitosan composite for the selective and sensitive electrochemical detection of Hg²⁺ in fish muscle. *Microchem. J.* **2022**, *175*, 107138. [[CrossRef](#)]
50. Wang, L.Y.; Yang, Y.X.; Liang, H.H.; Wu, N.; Peng, X.; Wang, L.; Song, Y.H. A novel N,S-rich COF and its derived hollow N,S-doped carbon@Pd nanorods for electrochemical detection of Hg²⁺ and paracetamol. *J. Hazard. Mater.* **2021**, *409*, 124528. [[CrossRef](#)]